Materials Science in Semiconductor Processing 217 (2027) 111113

Contents lists available at ScienceDirect

Materials Science in Semiconductor Processing

journal homepage: www.elsevier.com/locate/mssp

Synergistic effect of thermal and light-soaking treatments on CZTSSe/ALD-ZTO solar cells

Carla Gobbo [a,1], Fabio Butrichi [a,1], Giorgio Tseberlidis [a,b,*], Valerio Di Palma [a], Berenice Elena Gaia Colombo [a], Vanira Trifiletti [a], Maurizio Acciarri [a], Simona Binetti [a]

[a] Department of Materials Science and Solar Energy Research Centre (MIB-SOLAR), University of Milano-Bicocca, Via Cozzi 55, Milan, 20125, Italy
[b] CNR-ISSMC Istituto di Scienza, Tecnologia e Sostenibilità per Lo Sviluppo Dei Materiali Ceramici, Via Granarolo 64, Faenza, RA, 48018, Italy

ARTICLE INFO

Keywords:
Kesterite
Zinc-tin-oxide
Cd-free buffer layer
Atomic layer deposition
Thermal treatment
Light soaking
Solar cells

ABSTRACT

Kesterite $Cu_2ZnSn(S,Se)_4$ (CZTSSe) is an attractive thin-film absorber based on earth-abundant and low-toxicity elements. Nevertheless, high-performance CZTSSe solar cells still typically employ CdS buffer layers, which pose significant limitations due to the hazardous nature of Cd and introduce parasitic absorption at short wavelengths. The use of alternative buffer layers is therefore crucial for further advancing this technology. Among the possible candidates, $Zn_xSn_{1-x}O$ (ZTO) has emerged as a promising option due to its wide, tunable bandgap and benign constituents. In this work, ZTO buffer layers were deposited by Atomic Layer Deposition (ALD) at three different temperatures (150, 120, 90 °C). However, the as-deposited ZTO films exhibited high resistivity, which was mainly attributed to the controversial role of defect-related intragap states. To overcome this limitation, complete photovoltaic (PV) devices were annealed in air at 260 °C and subsequently exposed to light soaking. These post-deposition treatments synergistically improved the electrical conductivity of ZTO and reduced trap-assisted recombination, thereby enhancing final PV performance. Optical characterisation revealed a widened bandgap compared to conventional CdS, effectively suppressing parasitic absorption in the blue spectral region and enhancing short-circuit current density (J_{SC}) as expected. The best-performing devices were obtained with ZTO deposited at 90 °C, yielding efficiencies (η) exceeding 7% by optimising the trade-off between junction quality and ZTO conductivity. These experimental findings are corroborated by numerical SCAPS simulations and confirm the potential of ALD-grown ZTO as a Cd-free buffer layer for kesterite solar cells.

1. Introduction

Achieving a sustainable energy transition requires photovoltaic (PV) technologies based on materials that combine high efficiency, cost-effectiveness, and earth-abundant constituents. Among the possible candidates, kesterite $Cu_2ZnSn(S,Se)_4$ (CZTSSe) is particularly attractive, thanks to its high absorption coefficient (over 10^4 cm^{-1}), direct, tunable bandgap, and an environmentally benign, low-cost composition [1–4]. However, high-performance CZTSSe solar cells, with record efficiencies (η) above 16% [5], typically employ CdS buffer layers [6–9], which present several intrinsic limitations. In particular, the toxicity of Cd raises sustainability concerns, while its relatively narrow bandgap (E_g = 2.4-2.5 eV) results in parasitic absorption losses at short wavelengths [10,11]. Moreover, CdS exhibits a non-ideal band alignment with kesterites, thereby contributing to the open-circuit voltage (V_{OC}) deficit, one of the major drawbacks limiting kesterite technology [12–14]. Additional constraints arise from the considerable lattice mismatch at the CZTSSe/CdS interface (~2.4%), which promotes interfacial defect formation and reduces device performance [15]. Lastly, CdS is commonly deposited via chemical bath deposition (CBD), a technique that is highly sensitive to deposition conditions and may suffer from limited reproducibility and non-uniform film formation, often resulting in buffer layers with significant roughness, pinholes, and particle agglomeration [10,16]. These issues have driven intensive research toward the development of Cd-free buffer materials, including $Zn_xSn_{1-x}O$ (ZTO), Zn(O,S), ZnS, In_2S_3, and TiO_2 [10,17–19]. While

This article is part of a special issue entitled: GADEST 2026 published in Materials Science in Semiconductor Processing.

* Corresponding author. Department of Materials Science and Solar Energy Research Centre (MIB-SOLAR), University of Milano-Bicocca, Via Cozzi 55, 20125, Milan, Italy.
E-mail address: giorgio.tseberlidis@unimib.it (G. Tseberlidis).

[1] These authors contributed equally to this work.

https://doi.org/10.1016/j.mssp.2026.111113
Received 28 May 2026; Received in revised form 7 August 2026; Accepted 21 August 2026
Available online 25 August 2026

Table 1
Photovoltaic parameters of the Na-ACZTSSe/CdS reference solar cells, including the statistical average with standard deviation, the champion cell, and the representative device selected as the baseline for numerical SCAPS simulations.

CdS-based devices	J_{SC} (mA/cm^2)	V_{OC} (mV)	FF (%)	η (%)
Average	32 ± 3	399 ± 7	55 ± 1	7.3 ± 0.7
Champion cell	39	400	53	8.3
Representative cell (used for simulations)	34	396	56	7.4

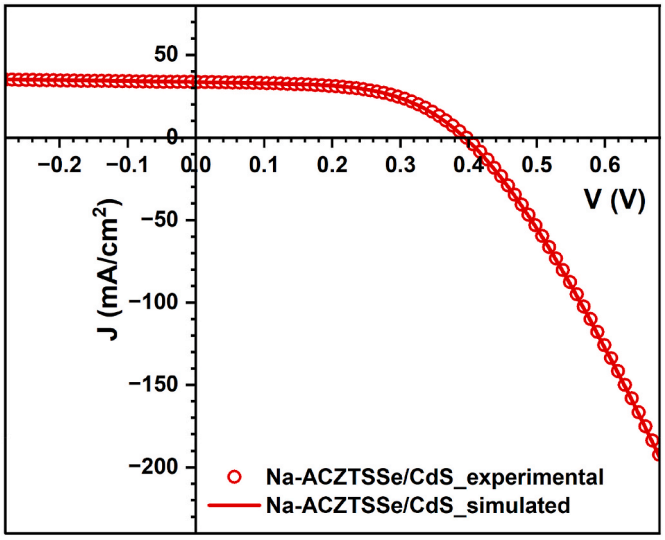

Fig. 1. Comparison between the simulated (solid line) and experimental (red dots) J-V curves of the representative CdS-based control device. (For interpretation of the references to colour in this figure legend, the reader is referred to the Web version of this article.)

alternatives like Zn(O,S) (η_{max} = 9.8%) [20], In_2S_3 (η_{max} = 7.6%) [21], and TiO_2 (η_{max} = 9.7%) [22] have shown promise when coupled with CZTSSe, their widespread application is constrained by the use of expensive elements such as In and modest efficiencies compared to CdS (η_{max} = 16.6%) [5] and ZTO (η_{max} = 13.9%) [23]. In this context, ZTO has emerged as the most promising candidate due to its earth-abundant, non-toxic composition and its wide, tunable bandgap (2.6 - 3.5 eV), which is beneficial for both enhancing light harvesting and improving band alignment [10,11,24]. The main techniques used to deposit high-quality ZTO buffer layers are sputtering and Atomic Layer Deposition (ALD). While sputtering allows for faster deposition rate and lower cost [25], ALD ensures precise control of stoichiometry and thickness, as well as high reproducibility and excellent uniformity [26–31]. Furthermore, the development of high-throughput variants, such as Spatial ALD (SALD) and Atmospheric Pressure Spatial ALD (AP-SALD), makes ALD-ZTO potentially scalable and applicable for industrial production [32].

As a result, several groups have optimised ALD-ZTO buffer layers for kesterite solar cells. In 2016, Li et al. reported the first investigation on ALD-ZTO in CZTSSe devices, studying the influence of buffer layer composition and thickness on PV performance [28]. In 2023, Ahmad et al. improved the band alignment at the p-n junction and facilitated charge extraction by combining ALD-ZTO with Ag-alloyed CZTSSe (ACZTSSe) [30]. More recently, it has become evident that, beyond optimisation of the buffer layer itself, further improvements require careful engineering of the kesterite/ZTO interface. Indeed, the presence of several defects at the CZTSSe/ZTO junction causes significant interfacial recombination losses, thereby reducing PV performance, particularly through decreases in V_{OC} and fill factor (FF) [23]. Considering the beneficial effect of heterojunction treatment previously demonstrated for CZTSSe/CdS devices, Zhao et al., in 2026 investigated the effect of a 200 °C annealing treatment on the CZTSSe/ZTO interface [23]. Similar to the behaviour observed in CdS-based samples, the thermal treatment promoted favourable elemental interdiffusion at the absorber/buffer interface, resulting in defect passivation and improved band alignment. Consequently, non-radiative recombination mediated by interfacial defects was significantly reduced, while carrier transport across the p-n junction was enhanced. While ALD-ZTO buffer layers have already enabled high-efficiency kesterite devices [23,30], a deeper understanding of their defects and transport properties is still required. In this work, we investigate the optical, electrical, and defect-related properties of ALD-ZTO thin films and evaluate their integration in CZTSSe solar cells, comparing them directly with control CdS-based devices processed under the same conditions. Specifically, the synergistic effect of thermal treatment (TT) combined with light soaking (LS) on Na-doped and Ag-alloyed CZTSSe (Na-ACZTSSe)/ZTO devices has been investigated. First, a SCAPS model (thoroughly described in the following sections and in the Supplementary Material File) of the experimental CZTSSe/CdS reference solar cell was used to determine the kesterite defectivity. Then, the CdS buffer layer was replaced with ZTO in the simulations to identify the optimal ZTO stoichiometry and thickness. Therefore, ZTO buffer layers Zn/Sn = 4 were deposited via ALD at three different temperatures (150, 120, and 90 °C). However, substituting CdS with ZTO was not enough, due to the high resistivity of the as-deposited ZTO films, which was mainly attributed to the controversial role of defect-related intragap states and the presence of defect states at the heterojunction interface. To address these limitations, complete PV devices were subjected to thermal treatment in air at 260 °C, followed by light soaking, which improved the electrical conductivity of ZTO and reduced trap-assisted recombination. Optical measurements confirmed the wider bandgap of ZTO compared with CdS, resulting in enhanced absorption in the blue region and higher short-circuit current density (J_{SC}). PV characterisation revealed that the ALD growth temperature also strongly influences device performance, especially fill factor (FF) and open-circuit voltage (V_{OC}), highlighting the critical role of deposition conditions on the absorber/buffer interface quality. The best results ($\eta > 7\%$) were obtained for ZTO deposited at 90 °C, which provided the best balance between preserving the junction and improving the ZTO conductivity. The efficiencies obtained are in agreement with numerical simulations, confirming the feasibility of using ZTO for Cd-free kesterite solar cells.

2. Methods

2.1. Device preparation

Commercial Mo-coated SLG with a SiO_x barrier layer at the SLG/Mo interface was used as the substrate. The kesterite precursor solution was prepared in ambient air, following the methodology optimised elsewhere [33]. TU [2.76 M], CuCl [0.59 M], and AgCl [0.066 M] were first dissolved in 2-Methoxyethanol (MOE) under vigorous stirring at 80 °C, yielding a TU–Cu–Ag ink. Then, $SnCl_4$ [0.42 M], $Zn(CH_3CO_2)_2$ [0.46 M], and $NaClO_4 \bullet H_2O$ [0.05 M] were added. After complete dissolution, a 0.45 μm nylon membrane was used to filter the so-obtained solution, which was subsequently spin-coated in eight deposition times onto the substrates (4000 rpm for 30 s). Each deposited layer was dried on a hot plate at 300 °C to remove the solvent, forming a 1.1 μm Na-ACZTS precursor film. The resulting films were then annealed in a graphite box with Se pellets, yielding Na-ACZTSSe absorber films. The samples were then completed as PV cells. ZTO buffer layers were deposited by ALD using a PICOSUN R-200 Advanced system. ZTO deposition temperatures of 150, 120, and 90 °C were investigated. In all cases, deposition was preceded by 40 min of sample thermalisation. Diethylzinc [Zn$(C_2H_5)_2$, DEZ] and tetrakis-(diethylamino)tin (IV) [Sn$(N(CH_3)_2)_4$, TDMASn] were employed as Zn and Sn precursors, respectively, while

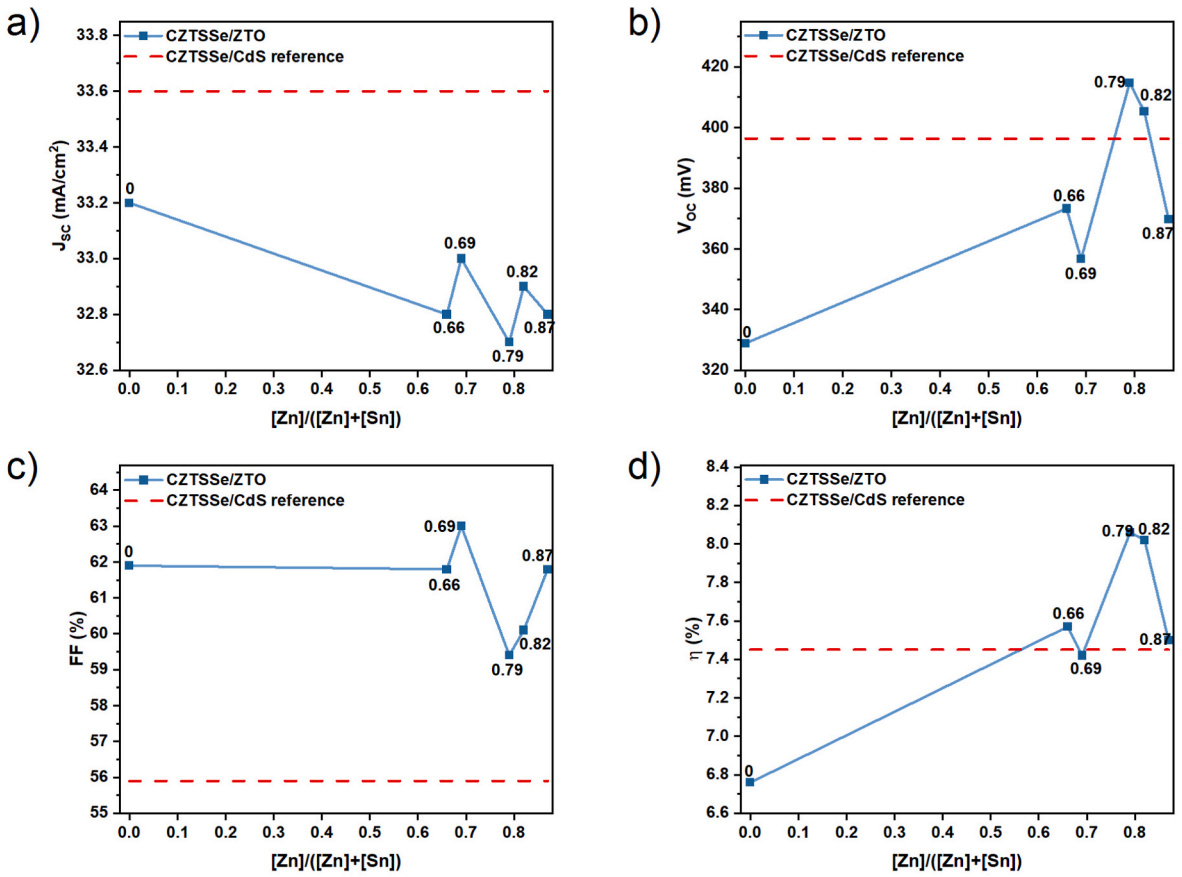

Fig. 2. Simulated values of a) J_{SC}, b) V_{OC}, c) FF and d) η of CZTSSe/ZTO junction as a function of ZTO stoichiometry.

Milli-Q H_2O was used as co-reactant and high-purity N_2 (99.9999%) as gas carrier. DEZ and Milli-Q H_2O were maintained at 22 °C using Peltier cooling during the entire deposition process, while TDMASn was heated to 75 °C. To avoid precursor condensation, the TDMASn line from the precursor container to the deposition chamber was maintained at 80 °C for the process at 90 °C, 90 °C for the deposition at 120 °C, and 95 °C during the deposition at 150 °C. The ZTO films were grown following a super-cycle scheme consisting of alternated depositions of ZnO and SnO_x, with a ZnO/SnO (Zn/Sn) cycle ratio of 4:1, a nominal growth per super-cycle of 0.34 nm, and a final thickness of 20 nm. Each ALD cycle consisted of the sequence DEZ/TDMASn dosing:N_2 purging:H_2O dosing:N_2 purging, with pulse durations of 0.1/0.6:6:0.1:6 s. The carrier gas flow was set to 150 sccm for N_2, DEZ, and H_2O, while TDMASn was delivered at 200 sccm, with a 400 sccm boost in the first 0.4 s. In the control devices, an 80 nm CdS layer was deposited by CBD to form the p-n junction. All the devices were completed with AZO (350 nm) deposited by DC pulsed (2 kHz) magnetron sputtering and with 300 nm-thick thermally evaporated Al grids. Only the reference devices also included an 80 nm i-ZnO layer deposited by RF magnetron sputtering between CdS and AZO layers, following the standard device process described elsewhere [34]. As demonstrated in our previous study [24], the i-ZnO layer is not only redundant but also detrimental when combined with ALD-grown ZTO buffer layers. Finally, the devices were manually scribed into individual cells with an active area of 0.16 cm^2. The complete ZTO-based devices were then annealed at 260 °C for 10 min and subjected to light soaking until the PV performance converged to stable plateau values.

2.2. Characterisation

Structural properties of ZTO were analysed by XRD using a Rigaku Miniflex 600 apparatus with a Cu Kα radiation ($\lambda = 1.5446$ Å) generated at 40 kV and 15 mA, with a silicon array detector in a Bragg Bentano geometry and θ-2θ configuration. ALD-grown ZTO film thicknesses were measured via spectroscopic ellipsometry using a Film Sense FS-1. The optical constants were modelled using a Tauc-Lorentz oscillator. J-V characteristics and light soaking measurements were performed under standard conditions using a Keithley 2460 source meter in combination with a 500 W xenon lamp (ABET Technologies Sun 2000 class ABA Solar Simulator). The ZTO's resistivity (ρ) was derived using the relation $\rho = R_{sheet} \bullet d$, where d is the thickness of the film, and R_{sheet} is the sheet resistance. R_{sheet} was measured on square-shaped ZTO films deposited on borosilicate glass using the Van der Pauw method [35]. A constant current was applied using a Keithley electrometer, and the resulting voltage was recorded. Each measurement was repeated three times to ensure the reliability of the results. Electrical contacts were formed at the four corners of the samples using silver paste. Optical transmittance spectra of ZTO films deposited on borosilicate glass were measured using a Jasco V-570 UV–Vis spectrophotometer. External quantum efficiency (EQE) spectra were recorded under AC conditions with an optical chopper operating at 78 Hz using a SpeQuest system. Wavelength selection was carried out with an Omni 300 LOT ORIEL Czerny-Turner single-grating monochromator. The system was calibrated using Si and Ge photodiodes. Photoluminescence (PL) measurements were performed using an Agilent Cary Eclipse fluorescence spectrophotometer. Spectra were recorded using a Xe lamp (power = 75 kW) at an excitation wavelength of 275 nm over an emission range of 320–750 nm, with excitation and emission slit widths of 20 nm.

2.3. Device simulation

The solar cell modelling was performed using SCAPS-1D software,

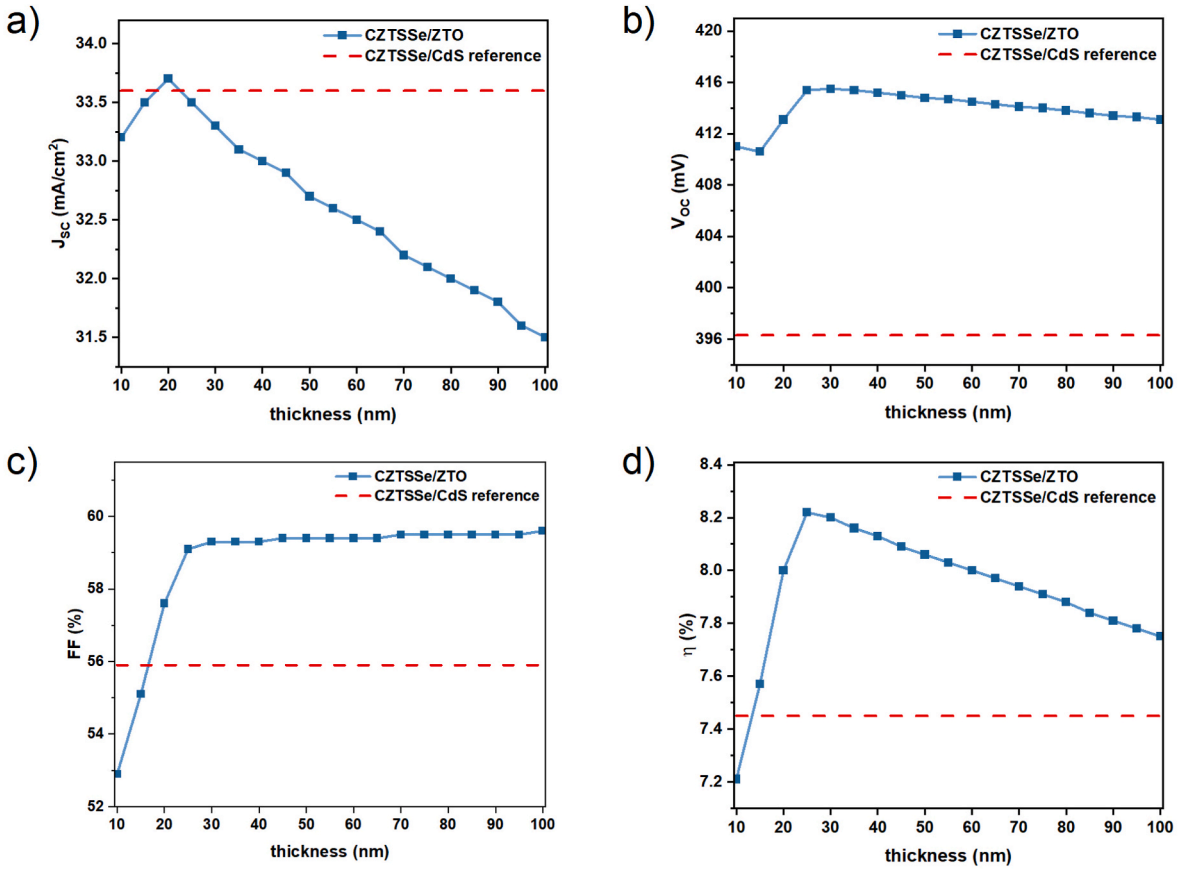

Fig. 3. Simulated values of a) J_{SC}, b) V_{OC}, c) FF and d) η of CZTSSe/ZTO junction as a function of ZTO thickness. The ZTO composition was fixed to Zn/Sn = 4.

developed at the Department of Electronics and Information Systems, University of Gent, by M. Burgelman et al. [36]. The software, based on the electron and hole continuity equations and the Poisson equation, is used to simulate the J-V characteristic of solar cell architectures. Each layer of the device is defined by its thickness, optoelectronic properties, and defect states. Defects at the interfaces can also be included. The numerical simulations were performed under standard conditions, with a temperature of 25.0 °C, an illumination power density of 100 mW cm^{-2}, and an air mass of 1.5.

3. Results and discussion

Reference devices employing a conventional CdS buffer layer were initially fabricated, and their PV parameters are summarised in Table 1. To establish a reliable baseline for the numerical model, a representative Na-ACZTSSe/CdS solar cell exhibiting near-average performance (J_{SC} = 34 mA/cm^2, V_{OC} = 396 mV, FF = 56%, η = 7.4%) was selected. The experimental J-V characteristic of this solar cell was subsequently simulated and fitted to derive the optoelectronic parameters and gain insights into the bulk and interface defectivity of the Na-ACZTSSe absorber. The simulation was performed considering Mo/$MoSe_2$/Na-ACZTSSe/CdS/i-ZnO/AZO/Al grid device architecture.

In the simulation, the kesterite bandgap (E_g) was fixed at 1.1 eV [4]. Since the p-type doping of the Na-ACZTSSe is largely governed by copper vacancies (V_{Cu}), and therefore depends on the Cu content of the absorber, a doping density on the order of 10^{16} cm^{-3} was assumed [37], considering both the precursor metal composition and the influence of alkaline doping. The remaining optoelectronic parameters were carefully selected from the literature [38,39] and subsequently fine-tuned to match the experimental J-V curve. The complete set of kesterite parameters used in the simulations is reported in Table S1. The kesterite bulk defectivity was defined based on extensive analysis of Deep-Level Transient Spectroscopy (DLTS) data reported in the literature for CZTSSe [40–45]. The energy level of each defect was determined as the average value reported across different studies, while the density and the capture cross section were adjusted to match the experimental characteristics of the reference device. Since Cu_{Zn}, together with V_{Cu}, are the most common intrinsic defects in the kesterite absorbers [46], their density was assumed to be two orders of magnitude higher than that of other defects. As the effect of V_{Cu} was already accounted for through the absorber doping density, V_{Cu} was not explicitly included in the defect list. The complete set of CZTSSe defect parameters used in the simulation is reported in Table S2. The optoelectronic parameters of the other layers of the solar cell ($MoSe_2$, CdS, i-ZnO and AZO) were selected from the literature [24,38,39,47] and are reported in Table S3. To improve simulation accuracy, interface defect states at the CZTSSe/CdS heterojunction were also included (Table S4). The interfacial defectivity was constructed considering two different contributions. In "Interface Defect 1", the potential presence of voids, interstitials and grain boundaries at the interface was modelled with a gaussian energy distribution [48]. On the other hand, "Interface Defect 2", built with a valence band tail energy distribution, accounts for the electrostatic fluctuations due to the band tailing phenomenon in kesterites [49]. The comparison between the simulated and experimental J-V curves of the selected reference device is reported in Fig. 1.

The simulated J-V curve (solid line) shows excellent agreement with the experimental reference solar cell (red dots). The series (R_S) and shunt (R_{SH}) resistances were extracted from the numerical fitting of the experimental J-V curve, yielding values of R_S = 0.93 Ω cm^2 and $R_{SH} = 1.0 \bullet 10^3$ Ω cm^2. Subsequently, the CdS buffer layer was replaced with ZTO in the simulation to predict the performance of the CZTSSe/ZTO heterojunction and identify the optimal ZTO composition, while maintaining the same kesterite parameters and the same interfacial defects. The i-ZnO layer was removed from the solar cell architecture, as

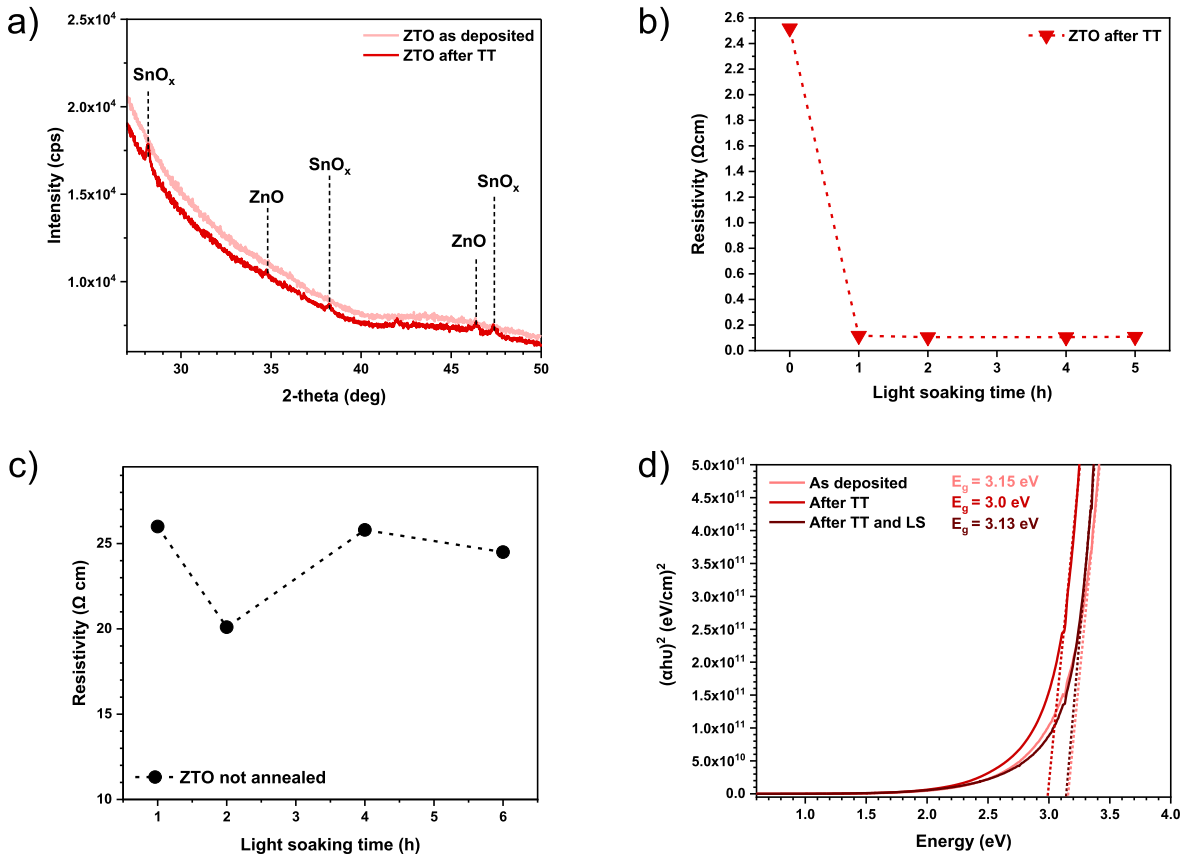

Fig. 4. (a) XRD patterns of ZTO as deposited and after TT in air at 260 °C for 10 min, reporting amorphous character and improved crystallinity, respectively. Evolution of resistivity during LS for ZTO films (b) with and (c) without TT, evidencing trap saturation effects. (d) Optical bandgap of ZTO films (as deposited, after TT, and after TT and LS).

previous studies have reported its detrimental effect when combined with the kesterite/ZTO junction [24]. Since the ZTO composition, which can be modulated by tuning the Zn:Sn ratio, alters the final properties of the buffer layer (e.g., band alignment, band gap, electron affinity) and consequently the PV performance, a compositional simulation study was performed to determine the best stoichiometry. The band gap and electron affinity values used for each composition are reported in Table S5 and derived from the literature [50,51]. The remaining opto-electronic parameters of ZTO were carefully selected and adapted from literature [24,52,53] and summarised in Table S6. The simulated PV parameters of the CZTSSe/ZTO devices as a function of ZTO composition are reported in Fig. 2. In this simulation, the ZTO thickness was fixed to 50 nm.

As shown in Fig. 2a, the simulated J_{SC} values for ZTO-based samples are slightly lower than those of the CdS reference device for all the investigated ZTO compositions. Nevertheless, J_{SC} could potentially be increased beyond the control device through suitable post-deposition treatments, as discussed in the following sections. A much stronger dependence on ZTO stoichiometry is observed for V_{OC} (Fig. 2b). Only ZTO compositions with a Zn/Sn ratio close to 4 are predicted to outperform the CdS reference, yielding V_{OC} values above 400 mV. In contrast, the other stoichiometries exhibit values in the 300-370 mV range, below the reference value of 396 mV. This behaviour can be attributed to the conduction band offset (CBO) at the kesterite/ZTO interface. An optimal charge transfer process requires a small and positive CBO; therefore, the variation of bandgap and electron affinity with ZTO composition has a significant impact on the achievable V_{OC}. The FF values obtained with ZTO are consistently higher than those of the reference CdS-based device for all the investigated compositions (Fig. 2c). As a result, the predicted efficiencies (η) reported in Fig. 2d are comparable to or higher than those with CdS. In particular, the ZTO-based devices with Zn/Sn ratio of approximately 4 are predicted to achieve the highest efficiency, thanks to the combination of high FF and V_{OC}. Then, the stoichiometry was fixed to Zn/Sn = 4, and the PV parameters of the CZTSSe/ZTO were simulated as a function of ZTO thickness; the results are reported in Fig. 3. The simulated V_{OC} is only weakly affected by the ZTO thickness, while J_{SC} is strongly dependent on it (Fig. 3a and b). The highest J_{SC} value, and the only one surpassing the reference device, is obtained for a ZTO thickness of 20 nm. The FF (Fig. 3c) increases gradually with ZTO thickness and exceeds the CdS reference value for thicknesses above 20 nm. Consequently, the simulated efficiency is higher than that of the reference device over a wide thickness range. The maximum efficiency of 8.22% is predicted for a 25 nm thick ZTO layer (Fig. 3d). It should be noted that the efficiency decrease associated with increasing ZTO thickness is likely underestimated in the present simulations. In SCAPS, the series and shunt resistances must be defined a priori and are not directly linked to the electrical properties of the simulated layers. As a result, the efficiency reduction observed at larger ZTO thicknesses mainly originates from increased bulk recombination within the buffer layer, while the additional losses associated with the higher electrical resistivity of thicker ZTO films are not fully captured. Nevertheless, the identification of a thin ZTO layer, around 20–25 nm, as the optimal thickness can be considered a robust outcome of the simulation study.

Based on the simulation results, a 20 nm-thick ZTO layer with a Zn:Sn ratio of 4:1 was identified as the most promising candidate and was therefore selected for the experimental investigation. The ZTO deposition temperature was set at 150 °C, consistent with the processing conditions previously optimised elsewhere [24]. First, the sheet resistance of the standalone ZTO films deposited on borosilicate glass was

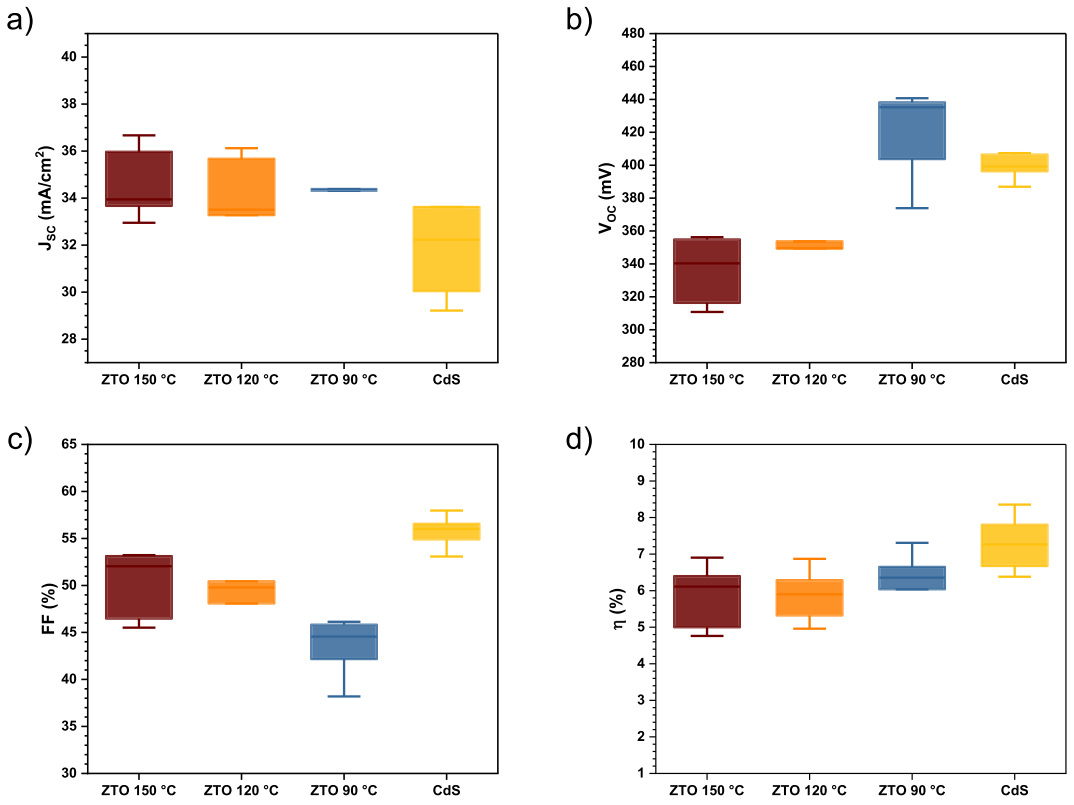

Fig. 5. Statistical distributions of (a) J_{SC}, (b) V_{OC}, (c) FF, and (d) η for kesterite solar cells with ZTO deposited by ALD at 150 °C (bordeaux), at 120 °C (orange), at 90 °C (blue), and with CdS (yellow). All PV parameters for the ZTO-based devices were measured after post-deposition treatments, both TT at 260 °C and LS. (For interpretation of the references to colour in this figure legend, the reader is referred to the Web version of this article.)

determined via the Van der Pauw method [35]. Nevertheless, the as-deposited ZTO layer exhibited high resistivity (>25 Ω cm), which is incompatible with efficient solar cell operation. Considering that post-deposition annealing can significantly influence the electrical properties of ZTO, often inducing a transition from semiconducting to metallic-like behaviour [54,55], the films were annealed in air at 260 °C for 10 min to optimise the trade-off between improved ZTO conductivity and thermal compatibility with the device stack. As a result, structural modification and defect-related changes were observed. While the as-deposited ZTO films showed an amorphous structure, with no well-defined diffraction pattern (Fig. 4a), the samples annealed in air revealed clear peaks related to ZnO and SnO_x. The formation of such nanocrystallites in the ZTO matrix reduces structural disorder, thereby improving carrier mobility and enhancing charge transport. Indeed, the film resistivity was reduced by an order of magnitude to 2.52 Ω cm (Fig. 4b). Besides the improvements associated with the formation of crystalline domains and film densification, this resistivity drop is also governed by the complex role of intragap defect states (such as V_O) in ZTO, which can act as both shallow donors and scattering centres [56]. Annealing in air likely atomically rearranges ZTO and partially suppresses structural and chemical defects [57], thus mitigating carrier scattering and trapping. This defect passivation ultimately improves carrier mobility and, consequently, enhances the overall electrical conductivity. Electrical properties were further modulated via LS treatment (Fig. 4b), during which the ZTO films were exposed to a simulated AM1.5G solar spectrum for several hours. This procedure is known to temporarily saturate trap states in the buffer layer, thereby improving conductivity and device performance [58–61]. Under prolonged, continuous illumination, the photo-induced de-trapping of residual defect states increases the effective carrier concentration, working synergistically with the prior TT to drastically reduce the ZTO resistivity (Fig. 4b). The most significant change occurred during the first hour of illumination, with the resistivity decreasing by more than an order of magnitude, from 2.52 to 0.12 Ω cm. This parameter further dropped within the second hour, reaching a stable value of 0.10 Ω cm. This resistivity was then maintained with minor fluctuations over the subsequent LS treatment. For comparison, the effect of LS was also evaluated on as-deposited ZTO samples, as reported in Fig. 4c. In this case, the ZTO films exhibited higher resistivity, in the range of 20-25 Ω cm, suggesting that LS alone induces only marginal changes in the electrical conductivity. In contrast, its effectiveness is strongly enhanced when combined with prior TT. As shown in Fig. S1, extending the TT time to 20 min did not provide additional benefit when coupled with LS. Importantly, the wide bandgap of ZTO (3.0-3.15 eV), which ensures minimal parasitic absorption in the visible range compared to CdS and makes it suitable as a transparent buffer layer, was maintained after both TT and LS (Fig. 4d). On the other hand, while TT effect is permanent, LS beneficial effect seems to be reversible when no illumination is present, with very slow kinetics (over 18-24h), suggesting the involvement of intragap states saturating under illumination in normal operating conditions and discharging during a prolonged rest period in the dark as shown by PL measurements (Fig. S3) and conductivity measurements (Fig. S4). Overall, the synergistic effect of TT and LS suggests that these post-deposition treatments are key steps for optimising CZTSSe/ZTO solar cells. By significantly reducing the resistivity of the ZTO buffer layer, TT and LS can decrease the series resistance (R_S) of the device, thus improving charge collection and, consequently, enhancing both the short-circuit current density (J_{SC}) and fill factor (FF).

All the characterisation discussed above was performed on ZTO films grown by ALD on borosilicate glass. When sandwiched between the kesterite absorber and the AZO layer in the complete device architecture, ZTO is expected to exhibit minor variations in microstructural defects and electrical conductivity due to substrate-related effects and interactions at the interfaces involved. Consequently, the resistivity

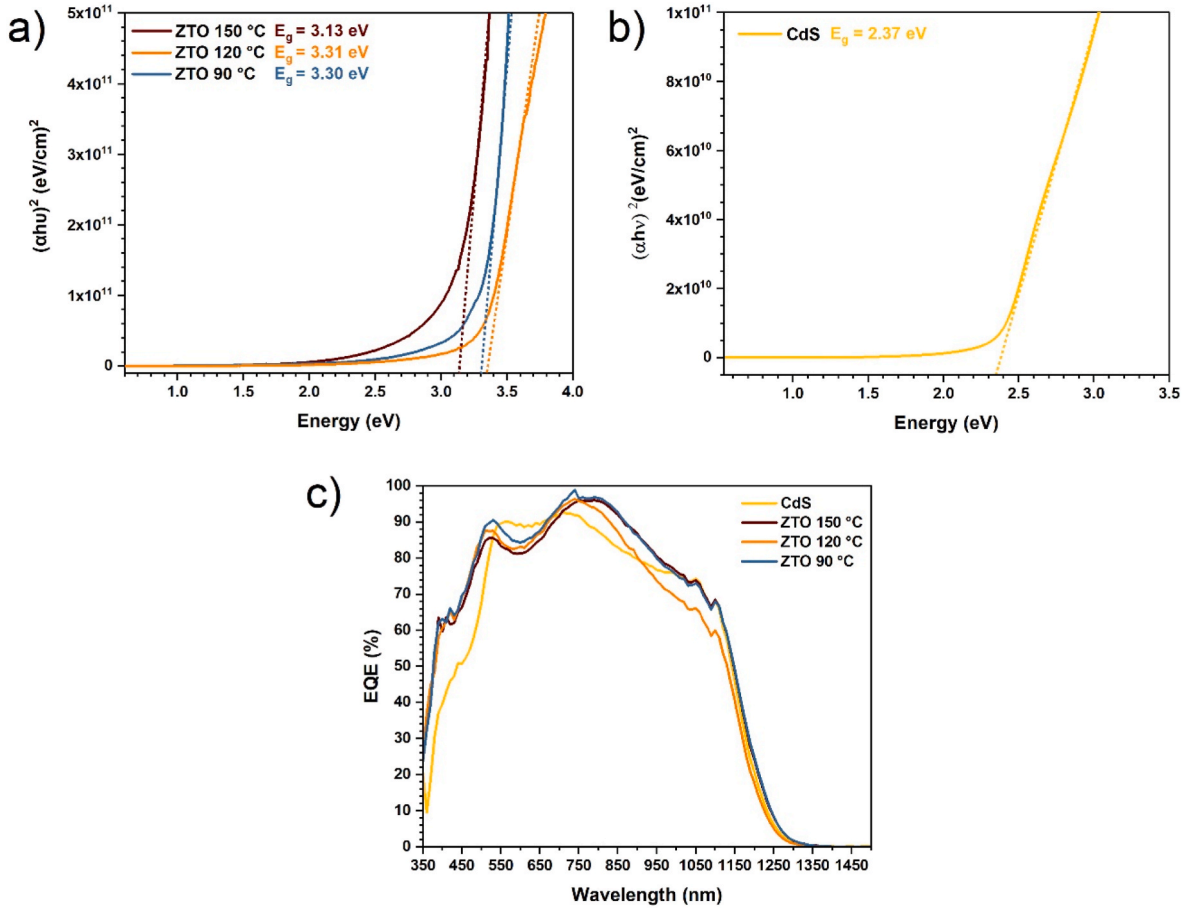

Fig. 6. Tauc's plot of (a) ZTO deposited at 150 °C (bordeaux), 120 °C (orange), 90 °C (blue), and (b) CdS. (c) EQE curves of the CdS-based and Cd-free devices. (For interpretation of the references to colour in this figure legend, the reader is referred to the Web version of this article.)

trends measured on glass serve as a qualitative useful reference rather than an exact representation of the ZTO behaviour in the final PV device. To evaluate device performance, ZTO films were subsequently deposited at 150 °C onto Na-ACZTSSe absorbers, whose material properties were consistent with those adopted in SCAPS simulations. Structural characterisation by XRD, complemented by Raman, carried out on the absorber, is reported in Fig. S2, confirming its quality and the absence of secondary phases. The resulting solar cells were subjected to TT and LS treatments. Compared to the reference devices employing CdS as the buffer layer, the lower efficiency of the ZTO-based solar cells was primarily attributed to their reduced open-circuit voltage (V_{OC}) (Fig. 5). Indeed, at a ZTO deposition temperature of 150 °C, the prolonged residence time in the ALD chamber may promote an excessive diffusion of Cu, Zn, Sn, and Se from the absorber layer into the growing ZTO film, leading to the formation of an intermixed interphase region at the p-n junction and the creation of recombination centres [62]. This thermally activated interdiffusion and elemental redistribution, which can be further enhanced during the subsequent TT, alters the local energy bandgap and the band alignment at the interface, potentially resulting in a cliff-like conduction band offset [63]. As reported in previous studies [26], such interface modification can increase surface recombination and reduce V_{OC}. This effect is expected to be particularly relevant considering the limited ZTO thickness of 20 nm, where even modest interdiffusion can significantly affect the p-n junction properties. Additionally, the prolonged exposure to 150 °C during ZTO-ALD deposition may further enhance the diffusion of Cu and Se toward the back contact, a phenomenon typically observed after the high-temperature selenisation process [64,65]. As a consequence, the formation of Sn- and Zn-related defects is favoured, thereby degrading the absorber/back contact interface and contributing to the observed reduction in V_{OC}. To mitigate these effects, ZTO was also deposited at lower temperatures of 120 and 90 °C. As reported in Fig. 5, devices with ZTO deposited at 120 °C exhibited PV performance comparable to those with ZTO deposited at 150 °C. In contrast, further reducing the deposition temperature to 90 °C resulted in an increase in V_{OC} of approximately 100 mV. These results support the hypothesis that milder ZTO deposition conditions improve the quality of the p-n junction by limiting severe interdiffusion and recombination losses. However, under these conditions, a reduction in FF was also observed. This behaviour can be related to interfacial transport limitations. Indeed, while lower ZTO deposition temperature suppresses detrimental interface degradation, it may also prevent the moderate intermixing and defect passivation beneficial for charge transport across the kesterite/ZTO junction [64]. Consequently, the series resistance is increased, and the electron extraction is less favourable, leading to a reduction in FF. Nevertheless, the significant gain in V_{OC} compensated for this effect, resulting in the highest PV efficiencies for devices employing ZTO deposited at 90 °C. All the Cd-free solar cells reported higher J_{SC} values than the reference devices (Fig. 5a). This improvement is consistent with the higher optical transparency of the ZTO films in the visible region as emerges from their transmittance measurements and the EQE collected on the corresponding Cd-free devices shown in Fig. 6. Indeed, compared with CdS, ZTO has a wider bandgap, which prevents parasitic absorption and allows more photons to reach the kesterite absorber layer, thereby enhancing photogeneration.

While TT and LS have been proven to be effective in modulating the ZTO conductivity, evaluating their impact on the complete solar cell stack, especially on the kesterite/buffer layer interface, is essential.

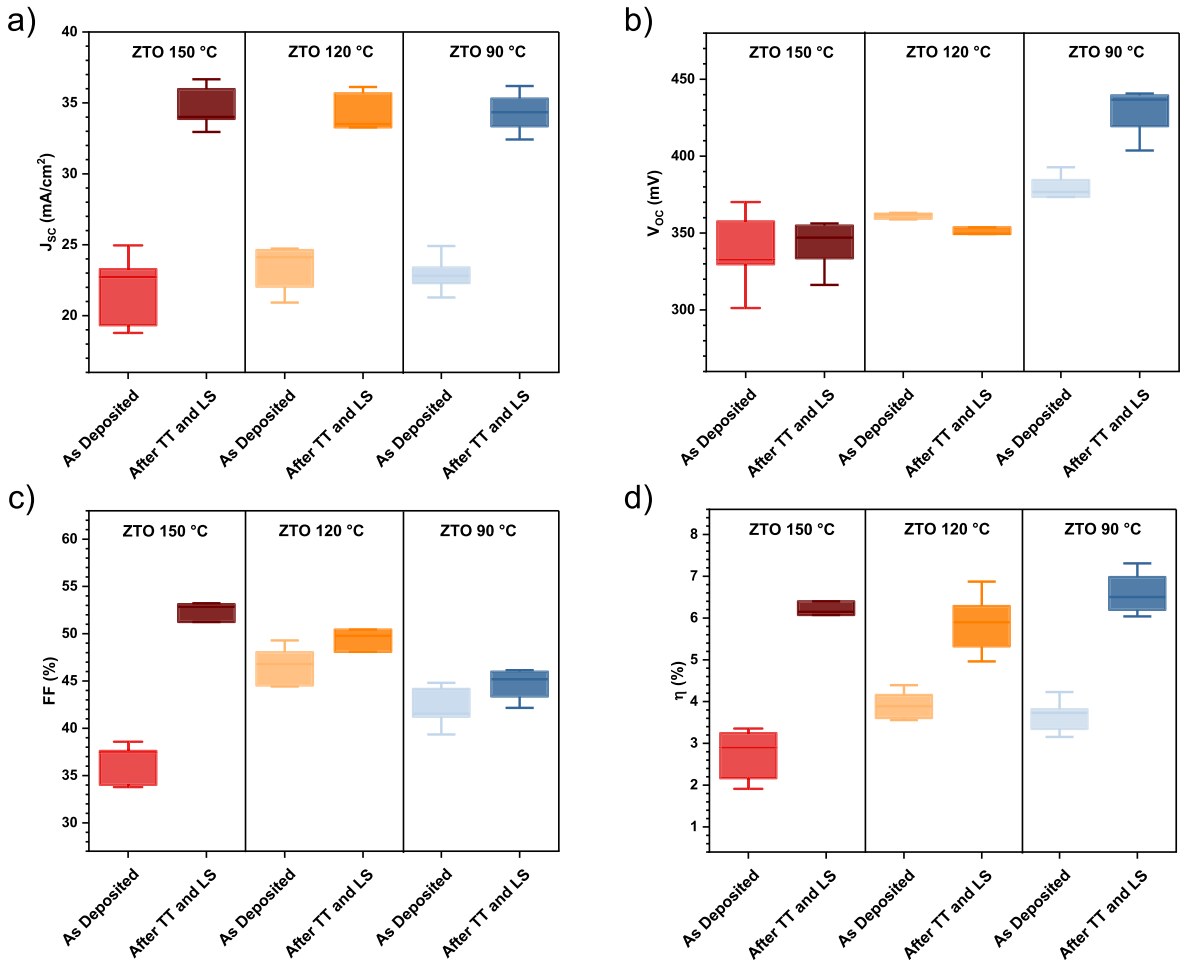

Fig. 7. Box plots of (a) J_{SC} (b) V_{OC}, (c) FF, and (d) η for Cd-free kesterite solar cells with ALD-ZTO deposited at 150 °C (in red), 120 °C (in orange), and 90 °C (in blue), with and without post-deposition thermal treatments. (For interpretation of the references to colour in this figure legend, the reader is referred to the Web version of this article.)

Table 2
PV performance of the ZTO-based kesterite solar cells. Reported values include the average, standard deviation, and the best-performing cell for all cases.

ZTO deposition conditions	Measured	J_{SC} (mA/cm²)	V_{OC} (mV)	FF (%)	η (%)
ALD 150 °C	As-deposited	22 ± 3 (23)	338 ± 27 (333)	36 ± 2 (37)	2.7 ± 0.6 (2.9)
	After TT + LS	35 ± 1 (37)	342 ± 17 (356)	51 ± 3 (53)	6.1 ± 0.7 (6.9)
ALD 120 °C	As-deposited	23 ± 2 (25)	361 ± 2 (362)	47 ± 1 (49)	3.9 ± 0.4 (4.4)
	After TT + LS	34 ± 3 (33)	351 ± 14 (372)	50 ± 4 (55)	5.9 ± 0.8 (6.9)
ALD 90 °C	As-deposited	23 ± 1 (23)	377 ± 14 (393)	42 ± 2 (41)	3.6 ± 0.4 (3.8)
	After TT + LS	34 ± 1 (36)	429 ± 17 (441)	45 ± 2 (46)	6.6 ± 0.5 (7.3)

Fig. 7 and Table 2 provide further insight into the effect of the combined post-deposition treatments on the PV parameters of the ZTO-based devices, helping to elucidate the results observed in Fig. 5. The corresponding representative J-V curves are shown in Fig. 8. The beneficial impact of TT and LS is evident for all the investigated ZTO deposition conditions. Indeed, regardless of the ZTO deposition temperature, the as-fabricated solar cells exhibited limited performance, primarily due to low J_{SC} values, in agreement with the limited conductivity of the as-synthesised buffer layer (Fig. 4). After the synergistic effect of TT and LS, J_{SC} increased significantly in all cases and converged to an average value of approximately 34 mA/cm², indicating that charge collection became more efficient once the electrical limitation of the ZTO buffer layer was solved (Fig. 7a and Table 2). Consequently, this confirms that the minor variations in V_{OC} and FF discussed above are mainly related to the distinct effects of the ALD deposition temperature on the absorber/buffer layer interface, rather than to intrinsic differences in the ZTO properties. This beneficial effect is consistent with both the improved buffer layer crystallinity, which reduces defect-related disorder, and the photo-induced de-trapping of residual defect states during LS. Specifically, as previously reported in the literature [23], TT can promote the selective diffusion of Zn ions from the ZTO buffer layer into the absorber, thereby compensating for both interfacial and bulk defects (e.g., V_{Cu} and Cu_{Zn}) typically present in CZTSSe [15]. As a consequence, defect-assisted recombination losses are mitigated, and the CZTSSe/ZTO band alignment is modulated [23]. Furthermore, this treatment has also been reported to induce the formation of a quasi-epitaxial absorber/-buffer interface, thus passivating interfacial defects and mitigating lattice distortion, which in turn suppresses carrier recombination and enhances charge transport and collection [66]. Moreover, under prolonged illumination, the density of trap centres decreases, thereby favouring more efficient carrier extraction. The FF was boosted especially for devices with ZTO deposited at higher temperatures (150 and 120 °C), while the V_{OC} was further enhanced in those with ZTO grown at

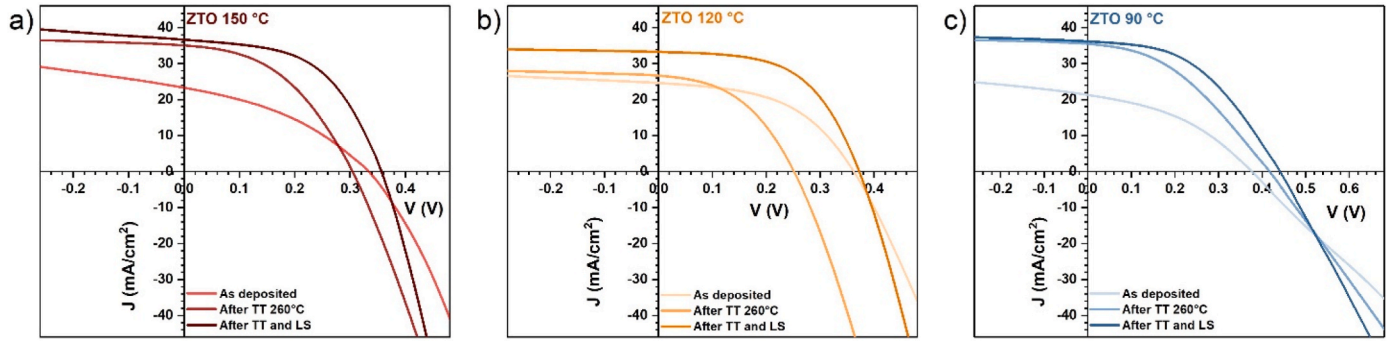

Fig. 8. J-V curves of CZTSSe/ZTO devices measured in the as-deposited state, after thermal treatment at 260 °C for 10 min, and after thermal treatment combined with light soaking, using buffer layers deposited at (a) 150 °C, (b) 120 °C, and (c) 90 °C.

90 °C (Fig. 7b and c). Overall, these results demonstrate that TT and LS are effective post-deposition optimisation steps for CZTSSe/ZTO solar cells. The final device performance is governed by the balance between preserving the absorber/buffer layer interface and improving the conducting properties of the ZTO. ZTO deposited at 90 °C provides the most advantageous overall compromise, yielding an η over 7% (Fig. 7d).

4. Conclusions

Overall, this work investigates the synergistic effect of TT and LS on CZTSSe/ZTO solar cells. First, a SCAPS model of the experimental Na-ACZTSSe/CdS reference device was used to deduce the defect parameters of the kesterite absorber. The CdS buffer layer was then replaced with ZTO in the simulations, identifying a Zn/Sn ratio of approximately 4 as the optimal ZTO stoichiometry, thanks to the combination of high FF and V_{OC} values. ZTO buffer layers with Zn/Sn = 4 were subsequently deposited via ALD at three different temperatures (150, 120, and 90 °C). Since substituting CdS with ZTO alone was insufficient to match the performance of the control device, post-deposition treatments were investigated, and their effect on both standalone ZTO films and complete solar cells was evaluated. TT improved the electrical conductivity of ZTO through the formation of crystalline domains and a likely reduction in the concentration of intra gap-related defect states, which act as carrier scattering and trapping centres. In addition, LS promoted photo-induced de-trapping of residual defect states, likely increasing the effective carrier concentration. The combined effect of TT and LS resulted in a significant reduction in ZTO resistivity and a corresponding improvement in device performance. Moreover, the ALD growth temperature was found to strongly influence PV parameters of the devices, particularly the FF and V_{OC} values, highlighting the critical role of deposition conditions on the kesterite/ZTO interface quality. The best-performing devices, fabricated with ZTO buffer layers deposited at 90 °C, achieved efficiencies exceeding 7%, representing the best compromise between preserving the p-n junction quality and improving the ZTO conductivity. The efficiencies obtained are consistent with numerical simulations, confirming the feasibility of Cd-free kesterite solar cells. In agreement with the literature, although the efficiency of these Cd-free devices still falls slightly behind our baseline CdS-based references, this work provides a clearer understanding of the defect nature and resistivity bottlenecks of ALD-ZTO. Identifying these material features is therefore crucial to bridge the gap with standard CdS buffer layers. These findings offer promising prospects for further optimisations and advancements in Cd-free kesterite solar cells.

CRediT authorship contribution statement

Carla Gobbo: Writing – review & editing, Writing – original draft, Visualization, Methodology, Investigation, Formal analysis, Data curation, Conceptualization. **Fabio Butrichi:** Writing – review & editing, Writing – original draft, Visualization, Methodology, Investigation, Formal analysis, Data curation, Conceptualization. **Giorgio Tseberlidis:** Writing – review & editing, Validation, Supervision, Methodology, Investigation, Conceptualization. **Valerio Di Palma:** Writing – review & editing, Validation, Methodology, Investigation, Conceptualization. **Berenice Elena Gaia Colombo:** Writing – review & editing, Investigation. **Vanira Trifiletti:** Writing – review & editing, Validation, Supervision. **Maurizio Acciarri:** Writing – review & editing, Supervision, Formal analysis. **Simona Binetti:** Writing – review & editing, Supervision, Resources, Project administration, Funding acquisition.

Declaration of competing interests

The authors declare that they have no known competing financial interests or personal relationships that could have appeared to influence the work reported in this paper.

Acknowledgements

This work was supported by the Italian Ministry of Environment and Energy Security in the framework of the Operating Agreement with ENEA for Research on the Electric System. The authors thank the research project “nuovi Concetti, mAteriali e tecnologie per l'iNtegrazione del fotoVoltAico negli edifici in uno scenario di generazione diffuSa” [CANVAS], funded by the Italian Ministry of the Environment and the Energy Security, through the Research Fund for the Italian Electrical System (type-A call, published on G.U.R.I. n. 192 on 18-08- 2022). The article is based upon work from COST Action Research and International Networking project “Emerging Inorganic Chalcogenides for PVs (RENEW-PV)," CA21148, supported by COST (European Cooperation in Science and Technology). F. B. acknowledges the Dottorato di Interesse Nazionale “Photovoltaics”.

Appendix A. Supplementary data

Supplementary data to this article can be found online at https://doi.org/10.1016/j.mssp.2026.111113.

Data availability

The authors confirm that the data supporting the findings of this study are available within the article or its Supplementary Information.

References

[1] M. He, C. Yan, J. Li, M.P. Suryawanshi, J. Kim, M.A. Green, X. Hao, Kesterite solar cells: insights into current strategies and challenges, Adv. Sci. 8 (2021) 2004313.
[2] A. Jimenez-Arguijo, Y. Gong, I. Caño, O. El Khouja, J. Li, K. Sun, Z. Jehl Li-Kao, S. Giraldo, H. Xin, A. Perez-Rodriguez, X. Hao, E. Saucedo, Formation pathway of high-efficiency kesterite solar cells fabricated through molecular ink chemistry, Nat. Energy 11 (2026) 194–208, https://doi.org/10.1038/s41560-025-01900-y.

[3] B.E.G. Colombo, A. Sangiorgi, G. Tseberlidis, C. Gobbo, F. Butrichi, V. Trifiletti, M. Acciarri, A. Sanson, S. Binetti, Above 10% efficiency flexible inkjet-printed kesterite solar cells, J. Energy Chem. 117 (2026) 880–892, https://doi.org/10.1016/j.jechem.2026.03.011.

[4] C. Gobbo, Y. Gong, A. Jimenez-Arguijo, G. Tseberlidis, V. Trifiletti, C. Malerba, M. Valentini, P. Estarlich, E. Armelin, S. Lanzalaco, R. Po, S. Binetti, E. Saucedo, Strategies for back contact engineering in high-performance flexible kesterite solar cells, J. Mater. Chem. A Mater 13 (2025) 25498–25508, https://doi.org/10.1039/D5TA03303A.

[5] M.A. Green, E.D. Dunlop, M. Yoshita, N. Kopidakis, K. Bothe, G. Siefer, X. Hao, J. Y. Jiang, Solar cell efficiency tables (version 67), Prog. Photovoltaics Res. Appl. 34 (2026) 482–496, https://doi.org/10.1002/pip.70068.

[6] J. Wang, F. Meng, L. Lou, K. Yin, X. Xu, M. Jiao, B. Zhang, Y. Li, J. Shi, H. Wu, Y. Luo, D. Li, Q. Meng, Vacancy-enhanced cation ordering via magnesium doping to enable kesterite solar cells with 14.9% certified efficiency, Nat. Energy 11 (2026) 66–75, https://doi.org/10.1038/s41560-025-01902-w.

[7] M. Jiao, B. Zhang, J. Wang, X. Xu, T. Guo, S. Chen, J. Wang, Y. Li, Y. Li, H. Wu, J. Shi, Y. Luo, D. Li, Q. Meng, Suppressing defects in kesterite solar cells via balanced phase evolution to enable 15.1% certified record efficiency, Joule 10 (2026), https://doi.org/10.1016/j.joule.2026.102345.

[8] X. Xu, J. Wang, M. Jiao, B. Zhang, T. Guo, Y. Li, J. Wang, S. Chen, Y. Li, D. Li, J. Shi, H. Wu, W. Yan, Y. Luo, Q. Meng, Alkali-metal-mediated control of phase segregation for flexible kesterite solar cells and modules with improved efficiency, Nat. Energy (2026), https://doi.org/10.1038/s41560-026-02018-5.

[9] H. Xu, N. Wang, R. Meng, X. Xu, S. Shao, J. Dong, J. Li, S. Wei, Z. Zhang, T. Li, H. Li, T. Xing, Y. Wang, M. Li, Y. Liu, Y. Zhang, Flexible CZTSSe thin-film solar cells with over 14% certified efficiency enabled by lithium doping, ACS Energy Lett. 11 (2026) 3916–3925, https://doi.org/10.1021/acsenergylett.6c00329.

[10] G. Tseberlidis, C. Gobbo, V. Trifiletti, V. Di Palma, S. Binetti, Cd-free kesterite solar cells: state-of-the-art and perspectives, Sustain. Mater. Technol. 41 (2024) e01003, https://doi.org/10.1016/j.susmat.2024.e01003.

[11] X. Cui, K. Sun, J. Huang, C.-Y. Lee, C. Yan, H. Sun, Y. Zhang, F. Liu, M. Hossain, Y. Zakaria, L. Wong, M. Green, B. Hoex, X. Hao, Enhanced heterojunction interface quality to achieve 9.3% efficient Cd-free Cu2ZnSnS4 solar cells using ALD ZnSnO buffer layer, Chem. Mater. 30 (2018), https://doi.org/10.1021/acs.chemmater.8b03398.

[12] R. Haight, A. Barkhouse, O. Gunawan, B. Shin, M. Copel, M. Hopstaken, D.B. Mitzi, Band alignment at the Cu2ZnSn(SxSe1−x)4/CdS interface, Appl. Phys. Lett. 98 (2011) 253502, https://doi.org/10.1063/1.3600776.

[13] A. Santoni, F. Biccari, C. Malerba, M. Valentini, R. Chierchia, A. Mittiga, Valence band offset at the CdS/Cu2ZnSnS4 interface probed by x-ray photoelectron spectroscopy, J. Phys. D Appl. Phys. 46 (2013) 175101, https://doi.org/10.1088/0022-3727/46/17/175101.

[14] M. Bär, B.-A. Schubert, B. Marsen, R.G. Wilks, S. Pookpanratana, M. Blum, S. Krause, T. Unold, W. Yang, L. Weinhardt, C. Heske, H.-W. Schock, Cliff-like conduction band offset and KCN-induced recombination barrier enhancement at the CdS/Cu2ZnSnS4 thin-film solar cell heterojunction, Appl. Phys. Lett. 99 (2011) 222105, https://doi.org/10.1063/1.3663327.

[15] H. Wei, Y. Li, C. Cui, X. Wang, Z. Shao, S. Pang, G. Cui, Defect suppression for high-efficiency kesterite CZTSSe solar cells: advances and prospects, Chem. Eng. J. 462 (2023) 142121, https://doi.org/10.1016/j.cej.2023.142121.

[16] A. Romeo, D.L. Bätzner, H. Zogg, C. Vignali, A.N. Tiwari, Influence of CdS growth process on structural and photovoltaic properties of CdTe/CdS solar cells, Sol. Energy Mater. Sol. Cell. 67 (2001) 311–321, https://doi.org/10.1016/S0927-0248(00)00297-X.

[17] C. Platzer-Björkman, N. Barreau, M. Bär, L. Choubrac, L. Grenet, J. Heo, T. Kubart, A. Mittiga, Y. Sanchez, J. Scragg, S. Sinha, M. Valentini, Back and front contacts in kesterite solar cells: state-of-the-art and open questions, J. Phys.: Energy 1 (2019) 044005, https://doi.org/10.1088/2515-7655/ab3708.

[18] A. Wang, M. He, M.A. Green, K. Sun, X. Hao, A critical review on the progress of kesterite solar cells: current strategies and insights, Adv. Energy Mater. 13 (2023) 2203046, https://doi.org/10.1002/aenm.202203046.

[19] Q. Sun, J. Tang, C. Zhang, Y. Li, W. Xie, H. Deng, Q. Zheng, J. Wu, S. Cheng, Efficient environmentally friendly flexible CZTSSe/ZnO solar cells by optimizing ZnO buffer layers, Materials 16 (2023) 2869, https://doi.org/10.3390/ma16072869.

[20] H. Jeong, R. Nandi, J.Y. Cho, P.S. Pawar, H.S. Lee, K.E. Neerugatti, J.H. Kim, J. Heo, CZTSSe/Zn(O,S) heterojunction solar cells with 9.82% efficiency enabled via (NH4)2S treatment of absorber layer, Prog. Photovoltaics Res. Appl. 29 (2021) 1057–1067, https://doi.org/10.1002/pip.3439.

[21] D.A.R. Barkhouse, R. Haight, N. Sakai, H. Hiroi, H. Sugimoto, D.B. Mitzi, Cd-free buffer layer materials on Cu2ZnSn(SxSe1−x)4: band alignments with ZnO, ZnS, and In2S3, Appl. Phys. Lett. 100 (2012) 193904, https://doi.org/10.1063/1.4714737.

[22] Z. Wang, Y. Wang, N. Taghipour, L. Peng, G. Konstantatos, Ag-Refined kesterite in superstrate solar cell configuration with 9.7% power conversion efficiency, Adv. Funct. Mater. 32 (2022) 2205948, https://doi.org/10.1002/adfm.202205948.

[23] Y. Zhao, S. Chen, J. Shi, S. Wang, J. Yang, Z. Su, Z. Zheng, H. Ma, X. Zhang, G. Liang, Intrinsic defect compensation in the space charge region enables cadmium-free kesterite solar cells to achieve 13.9% certified efficiency, Energy Environ. Sci. 19 (2026) 2356–2366, https://doi.org/10.1039/D6EE00550K.

[24] C. Gobbo, V. Di Palma, V. Trifiletti, C. Malerba, M. Valentini, I. Matacena, S. Daliento, S. Binetti, M. Acciarri, G. Tseberlidis, Effect of the ZnSnO/AZO interface on the charge extraction in Cd-Free kesterite solar cells, Energies 16 (2023) 4137, https://doi.org/10.3390/en16104137.

[25] B. Lin, Q. Sun, C. Zhang, H. Deng, Y. Li, W. Xie, Y. Li, Q. Zheng, J. Wu, S. Cheng, Efficient Cd-Free flexible CZTSSe solar cells with quality interfaces by using the Zn1–xSnxO buffer layer, ACS Appl. Energy Mater. 6 (2023) 1037–1045, https://doi.org/10.1021/acsaem.2c03541.

[26] J. Lee, T. Enkhbat, G. Han, M.H. Sharif, E. Enkhbayar, H. Yoo, J.H. Kim, S. Kim, J. Kim, Over 11 % efficient eco-friendly kesterite solar cell: effects of S-enriched surface of Cu2ZnSn(S,Se)4 absorber and band gap controlled (Zn,Sn)O buffer, Nano Energy 78 (2020) 105206, https://doi.org/10.1016/j.nanoen.2020.105206.

[27] S. Sinha, D.K. Nandi, S.-H. Kim, J. Heo, Atomic-layer-deposited buffer layers for thin film solar cells using earth-abundant absorber materials: a review, Sol. Energy Mater. Sol. Cell. 176 (2018) 49–68, https://doi.org/10.1016/j.solmat.2017.09.044.

[28] X. Li, Z. Su, S. Venkataraj, S.K. Batabyal, L.H. Wong, 8.6% efficiency CZTSSe solar cell with atomic layer deposited Zn-Sn-O buffer layer, Sol. Energy Mater. Sol. Cell. 157 (2016) 101–107, https://doi.org/10.1016/j.solmat.2016.05.032.

[29] J.Y. Cho, J.S. Jang, V.C. Karade, R. Nandi, P.S. Pawar, T.-J. Seok, W. Moon, T. J. Park, J.H. Kim, J. Heo, Atomic-layer-deposited ZnSnO buffer layers for kesterite solar cells: impact of Zn/(Zn+Sn) ratio on device performance, J. Alloys Compd. 895 (2022) 162651, https://doi.org/10.1016/j.jallcom.2021.162651.

[30] N. Ahmad, Y. Zhao, F. Ye, J. Zhao, S. Chen, Z. Zheng, P. Fan, C. Yan, Y. Li, Z. Su, X. Zhang, G. Liang, Cadmium-Free Kesterite thin-film solar cells with high efficiency approaching 12%, Adv. Sci. 10 (2023) https://doi.org/10.1002/advs.202302869.

[31] S.M. George, Atomic layer deposition: an overview, Chem. Rev. 110 (2010) 111–131, https://doi.org/10.1021/cr900056b.

[32] R.L.Z. Hoye, D. Muñoz-Rojas, Z. Sun, H. Okcu, H. Asgarimoghaddam, J. L. MacManus-Driscoll, K.P. Musselman, Spatial atomic layer deposition for energy and electronic devices, PRX Energy 4 (2025) 17002, https://doi.org/10.1103/PRXEnergy.4.017002.

[33] C. Gobbo, V. Trifiletti, G. Tseberlidis, Y. Gong, A. Jimenez-Arguijo, C. Boldrini, J. Barichello, L.A. Castriotta, Y. Raoui, P. Mariani, F. Matteocci, A. Di Carlo, P. Biagini, E. Saucedo, R. Po, S. Binetti, Demonstration of overcoming 20% efficiency in kesterite/perovskite tandem solar cells on rigid and flexible substrates, Commun. Mater. (2026), https://doi.org/10.1038/s43246-026-01213-x.

[34] G. Tseberlidis, A. Hasan Husien, S. Riva, L. Frioni, A. Le Donne, M. Acciarri, S. Binetti, Semi-transparent Cu2ZnSnS4 solar cells by drop-casting of sol-gel ink, Sol. Energy 224 (2021) 134–141, https://doi.org/10.1016/j.solener.2021.05.073.

[35] L.J. van der Pauw, A method of measuring specific resistivity and HALL effect of discs of arbitrary shape, in: Semiconductor Devices: Pioneering Papers, WORLD SCIENTIFIC, 1991, pp. 174–182, https://doi.org/10.1142/9789814503464_0017.

[36] M. Burgelman, P. Nollet, S. Degrave, Modelling polycrystalline semiconductor solar cells, Thin Solid Films (2000) 361–362, https://doi.org/10.1016/S0040-6090(99)00825-1, 527–532.

[37] G. Ren, D. Zhuang, M. Zhao, Y. Wei, Y. Wu, X. Li, X. Lyu, C. Wang, L. Hu, J. Wei, Q. Gong, Influences of Cu concentration on electrical properties of CZTSSe absorbers and their device performances, Vacuum 173 (2020) 109121, https://doi.org/10.1016/j.vacuum.2019.109121.

[38] A. Cherouana, R. Labbani, Study of CZTS and CZTSSe solar cells for buffer layers selection, Appl. Surf. Sci. 424 (2017) 251–255, https://doi.org/10.1016/j.apsusc.2017.05.027.

[39] Y. Putthisigamany, K.S. Rahman, M.M.I. Sapeli, N. Ahmad Ludin, M. AdibIbrahim, P. Chelvanathan, Revealing the subtle role of DC-Sputtered Mo back contact work function in mitigating the detrimental effects of the MoS2/MoSe2 interfacial layer in kesterite-based thin film solar cells, Energy & Fuels 38 (2024) 11188–11203, https://doi.org/10.1021/acs.energyfuels.4c00512.

[40] X. Chen, Y. Zhao, N. Ahmad, J. Zhao, Z. Zheng, Z. Su, X. Peng, X. Li, X. Zhang, P. Fan, G. Liang, S. Chen, Achieving high open-circuit voltage in efficient kesterite solar cells via lanthanide europium ion induced carrier lifetime enhancement, Nano Energy 124 (2024) 109448, https://doi.org/10.1016/j.nanoen.2024.109448.

[41] S. Das, S.K. Chaudhuri, R.N. Bhattacharya, K.C. Mandal, Defect levels in Cu2ZnSn(SxSe1−x)4 solar cells probed by current-mode deep level transient spectroscopy, Appl. Phys. Lett. 104 (2014) 192106, https://doi.org/10.1063/1.4876925.

[42] Y. Qi, N. Wei, Y. Li, D. Kou, W. Zhou, Z. Zhou, Y. Meng, S. Yuan, L. Han, S. Wu, Passivating Sn $_{Zn}$ defect and optimizing energy level alignment via organic silicon salt incorporation toward efficient solution-processed CZTSSe solar cells, Adv. Funct. Mater. 34 (2024), https://doi.org/10.1002/adfm.202308333.

[43] T. Xie, L. Han, L. Chu, M. Han, Y. Jian, J. Chi, X. Zhong, T. Liu, D. Kou, W. Zhou, Z. Zhou, S. Yuan, Y. Meng, Y. Qi, S. Wu, Passivation of deep-level defects through chemical environment regulation for efficient CZTSSe solar cells based on active selenium adsorption–desorption process, Adv. Funct. Mater. 35 (2025), https://doi.org/10.1002/adfm.202414940.

[44] H. Geng, M. Wang, S. Wang, D. Kou, Z. Zhou, W. Zhou, Y. Qi, S. Yuan, L. Han, Y. Meng, S. Wu, Two-step cooling strategy for synergistic control of Cu $_{Zn}$ and Sn $_{Zn}$ defects enabling 12.87% efficiency (Ag,Cu) $_2$ ZnSn(S,Se) $_4$ solar cells, Adv. Funct. Mater. 33 (2023), https://doi.org/10.1002/adfm.202210551.

[45] Y. Gong, R. Qiu, C. Niu, J. Fu, E. Jedlicka, R. Giridharagopal, Q. Zhu, Y. Zhou, W. Yan, S. Yu, J. Jiang, S. Wu, D.S. Ginger, W. Huang, H. Xin, Ag incorporation with controlled grain growth enables 12.5% efficient kesterite solar cell with open circuit voltage reached 64.2% shockley–queisser limit, Adv. Funct. Mater. 31 (2021) 2101927, https://doi.org/10.1002/adfm.202101927.

[46] M.Y. Zaki, A. Velea, Recent progress and challenges in controlling secondary phases in Kesterite CZT(S/Se) thin films: a critical review, Energies 17 (2024) 1600, https://doi.org/10.3390/en17071600.

[47] H. Jalali, A.A. Orouji, I. Gharibshahian, Controlled conduction band offset in Sb2Se3 solar cell through introduction of (Zn,Sn)O buffer layer to improve photovoltaic performance: a simulation study, Sol. Energy Mater. Sol. Cell. 260 (2023) 112492, https://doi.org/10.1016/j.solmat.2023.112492.
[48] M. Kauk-Kuusik, K. Timmo, K. Muska, M. Pilvet, J. Krustok, R. Josepson, G. Brammertz, B. Vermang, M. Danilson, M. Grossberg, Detailed Insight into the CZTS/CdS Interface modification by air annealing in monograin layer solar cells, ACS Appl. Energy Mater. 4 (2021) 12374–12382, https://doi.org/10.1021/acsaem.1c02186.
[49] T. Gokmen, O. Gunawan, T.K. Todorov, D.B. Mitzi, Band tailing and efficiency limitation in kesterite solar cells, Appl. Phys. Lett. 103 (2013) 103506, https://doi.org/10.1063/1.4820250.
[50] S. Lee, S. Kim, S. Shin, Z. Jin, Y.-S. Min, Band structure of amorphous zinc tin oxide thin films deposited by atomic layer deposition, J. Ind. Eng. Chem. 58 (2018) 328–333, https://doi.org/10.1016/j.jiec.2017.09.045.
[51] A. Haddout, M. Fahoume, A. Raidou, M. Lharch, Numerical modeling of ZnSnO/CZTS based solar cells, Optoelectron, Letture 18 (2022) 276–282, https://doi.org/10.1007/s11801-022-1144-4.
[52] M. Saadat, O. Amiri, A. Rahdar, Optimization of (Zn,Sn)O buffer layer in Cu(In,Ga)Se2 based solar cells, Sol. Energy 189 (2019) 464–470, https://doi.org/10.1016/j.solener.2019.07.093.
[53] C. Zhang, Y. Li, B. Lin, J. Tang, Q. Sun, W. Xie, H. Deng, Q. Zheng, S. Cheng, Micro-mechanism study of the effect of Cd-free buffer layers ZnXO (X = Mg/Sn) on the performance of flexible Cu $_2$ ZnSn(S, Se) $_4$ solar cell, Chin. Phys. B 32 (2023) 028801, https://doi.org/10.1088/1674-1056/ac9b3a.
[54] A. Kaisha, D. Caffrey, A. Ainabayev, O. Toktarbaiuly, M. Ibraimov, H. Wang, N. Nuraje, I. V Shvets, Examining the desirable properties of ZnSnOy by annealing treatment with a real-time observation of resistivity, ACS Omega 9 (2024) 26205–26212, https://doi.org/10.1021/acsomega.4c01857.
[55] E. Rucavado, Q. Jeangros, D.F. Urban, J. Holovský, Z. Remes, M. Duchamp, F. Landucci, R.E. Dunin-Borkowski, W. Körner, C. Elsässer, A. Hessler-Wyser, M. Morales-Masis, C. Ballif, Enhancing the optoelectronic properties of amorphous zinc tin oxide by subgap defect passivation: a theoretical and experimental demonstration, Phys. Rev. B 95 (2017) 245204, https://doi.org/10.1103/PhysRevB.95.245204.
[56] N.-E. Sung, H.-K. Lee, K.H. Chae, J.P. Singh, I.-J. Lee, Correlation of oxygen vacancies to various properties of amorphous zinc tin oxide films, J. Appl. Phys. 122 (2017) 085304, https://doi.org/10.1063/1.5000138.
[57] J. Troughton, D. Atkinson, Amorphous InGaZnO and metal oxide semiconductor devices: an overview and current status, J. Mater. Chem. C Mater 7 (2019) 12388–12414, https://doi.org/10.1039/C9TC03933C.
[58] Z. Jiang, S. Soltanian, B. Gholamkhass, A. Aljaafari, P. Servati, Light-soaking free organic photovoltaic devices with sol–gel deposited ZnO and AZO electron transport layers, RSC Adv. 8 (2018) 36542–36548, https://doi.org/10.1039/C8RA07071G.
[59] L. Grenet, P. Grondin, K. Coumert, N. Karst, F. Emieux, F. Roux, R. Fillon, G. Altamura, H. Fournier, P. Faucherand, S. Perraud, Experimental evidence of light soaking effect in Cd-free Cu2ZnSn(S,Se)4-based solar cells, Thin Solid Films 564 (2014) 375–378, https://doi.org/10.1016/j.tsf.2014.05.033.
[60] M. Neuschitzer, Y. Sanchez, S. López-Marino, H. Xie, A. Fairbrother, M. Placidi, S. Haass, V. Izquierdo-Roca, A. Perez-Rodriguez, E. Saucedo, Optimization of CdS buffer layer for high-performance Cu2ZnSnSe4 solar cells and the effects of light soaking: elimination of crossover and red kink, Prog. Photovoltaics Res. Appl. 23 (2015) 1660–1667, https://doi.org/10.1002/pip.2589.
[61] S. Dhara, K.M. Niang, A.J. Flewitt, A. Nathan, S.A. Lynch, Tail state mediated conduction in zinc tin oxide thinfilm phototransistors under below bandgap optical excitation, Sci. Rep. 11 (2021) 19016, https://doi.org/10.1038/s41598-021-98339-4.
[62] J.-H. Wi, T.G. Kim, J.W. Kim, W.-J. Lee, D.-H. Cho, W.S. Han, Y.-D. Chung, Photovoltaic performance and interface behaviors of Cu(In,Ga)Se2 solar cells with a Sputtered-Zn(O,S) buffer layer by high-temperature annealing, ACS Appl. Mater. Interfaces 7 (2015) 17425–17432, https://doi.org/10.1021/acsami.5b04815.
[63] J. Lindahl, J. Keller, O. Donzel-Gargand, P. Szaniawski, M. Edoff, T. Törndahl, Deposition temperature induced conduction band changes in zinc tin oxide buffer layers for Cu(In,Ga)Se2 solar cells, Sol. Energy Mater. Sol. Cell. 144 (2016) 684–690, https://doi.org/10.1016/j.solmat.2015.09.048.
[64] Y. Li, C. Cui, H. Wei, Z. Shao, Z. Wu, S. Zhang, X. Wang, S. Pang, G. Cui, Suppressing element inhomogeneity enables 14.9% efficiency CZTSSe solar cells, Adv. Mater. 36 (2024), https://doi.org/10.1002/adma.202400138.
[65] F. Liu, J. Huang, K. Sun, C. Yan, Y. Shen, J. Park, A. Pu, F. Zhou, X. Liu, J.A. Stride, M.A. Green, X. Hao, Beyond 8% ultrathin kesterite Cu2ZnSnS4 solar cells by interface reaction route controlling and self-organized nanopattern at the back contact, NPG Asia Mater. 9 (2017), https://doi.org/10.1038/am.2017.103 e401–e401.
[66] P. Luo, S. Chen, G. Chen, M. Abbas, Z. Su, Z. Zheng, H. Ma, X. Zhang, G. Liang, Quasi-epitaxial heterojunction interface reconstruction enables 11.96% certified efficiency in Cd-free Cu2ZnSnS4 solar cells, Sci. Adv. 12 (2026), https://doi.org/10.1126/sciadv.aee0270 eaee0270.